Loading ultracold atoms onto nonlinear Bloch states and soliton states in bichromatic lattices

Tomotake Yamakoshi[1] and Shinichi Watanabe[2]

[1]*Institute for Laser Science, University of Electro-Communications, 1-5-1 Chofugaoka, Chofu-shi, Tokyo 182-8585, Japan*

[2]*Center for International Programs and Exchange, University of Electro-Communications, 1-5-1 Chofugaoka, Chofu-shi, Tokyo 182-8585, Japan*

(Received 18 March 2021; accepted 21 June 2021; published 9 July 2021)

We simulate and analyze an experimental method of loading interacting ultracold atoms onto nontrivial quantum states such as nonlinear Bloch wave and soliton solutions in a one-dimensional bichromatic lattice. Of standard bands, inverted bands, and bands with Dirac-like points permitted by a bichromatic lattice, we consider the case of an inverted band and examine the loading process in terms of nonlinear Bloch waves formed by an aggregate of ultracold atoms described by the mean-field model. Specifically, we solved the Gross-Pitaevskii equation numerically and found an appropriate standing wave-pulse sequence for the inverted band, which sequence proved to be a suitable protocol for producing soliton solutions. In addition, we examined the effect of an external potential and dynamical instabilities for the postloading process. We also provide an appropriate data set for future experimental realization of our findings.

DOI: 10.1103/PhysRevA.104.013309

I. INTRODUCTION

Recent advancements in experimental techniques with ultracold atoms, nonlinear optics, and exciton-polariton dynamics provide an excellent platform for studying wide varieties of nonlinear wave phenomena [1–3]. The Gross-Pitaevskii equation (GPE) well describes these systems [4] even though the GPE is based on the lowest-order mean-field approximation. Therefore, solving this equation expectedly allows us to draw analogies between different systems and investigate nonlinear phenomena in a wide range of parameter spaces. One of the most intriguing topics is the production and application of soliton solutions, namely, nondispersive localized wave packets [4,5]. An ultracold atomic system is suitable for studying nonlinear dynamics due to its high controllability and accessibility. One aspect is the dynamical control of external potential by varying the parameters of trapping lasers, magnetic coils, etc. Moreover, it is possible to alter the strength of atom-atom interaction via Feshbach resonance [6]. In the recent studies of ultracold atoms, dynamics of solitons [7,8] and soliton trains [9] were experimentally observed using an appropriate control of external potential to Bose-Einstein condensation (BEC). These results may pave the way, for instance, for constructing new types of soliton-based high-precision interferometers [10].

Another intriguing topic is nonlinear phenomena in the presence of a periodic potential [1]. The nonlinearity modifies the energy-band structure, namely, a general consequence of the periodic potential so that the now-well-known loop structure appears at a band edge [4,5]. In addition to this, the nonlinearity supports spatially localized solutions whose chemical potential lies between two allowed bands. They are referred to as "band-gap solitons" [11,12]. Some of these solutions are known to be described in terms of nonlinear Bloch waves (NBWs) [13]. Using periodic structures such as polariton condensation in a one-dimensional array of buried mesa traps [14], propagating light in a periodic Kerr nonlinear medium [2], and so forth, the NBWs are experimentally realized. In the nonlinear optics, time-periodic potentials are applied, and the solitons were measured in the time domain [15]. In the case of an ultracold atomic system, a spatially periodic potential such as an optical lattice (OL) [1] is applied by the interference of counterpropagating lasers. One of the significant advantages of such a system is that the periodic potential can be tuned in time with ease. This technique allows variation of the band structure, enabling the loading of atoms to a specific state. Indeed, in a recent experiment with a two-dimensional checkerboard lattice controlled by an acceleration of the atoms and staggered shift of the lattice, atoms were loaded to an NBW state located at the top of the loop in the ground band to observe its decay rate [16].

The ability to produce a specific target state coherently and efficiently is a prerequisite for achieving further applications. From a theoretical point of view, several techniques have been suggested, e.g., a fast-forward process [17], a mode-matching technique [18], and so forth. However, these techniques generally require some complex coherent control so that it is exceedingly challenging for experimental implementation. One of the very promising techniques applicable to the ultracold atomic lattice system is the "standing-wave pulse sequence method" [19–21], also known as the bang-bang (on-off) control [22]. Basically, it turns the optical lattice on and off with appropriate time intervals, which is a sequence of square pulses until the residual BEC wave function coincides with the targeted Bloch wave. An experimental group in Beijing applied this technique to one-, two-, and three-dimensional systems and demonstrated that the loading process is very efficient. Interestingly, they demonstrated

recently that the same technique goes beyond just preparing the initial state, but it would be capable of state-to-state manipulation in the manner of the Ramsey interferometry [23].

In our previous paper [24], we theoretically extended the experimental work of the standing-wave pulse method [19–21] to the bichromatic lattice system [25] in the linear regime. We also analyzed the selection rule and numerically optimized the time sequence using experimentally realizable parameters. Furthermore, we found that relatively weak nonlinear interaction (much smaller than lattice height) does not alter the selection rule and postloading dynamics since the band dispersion is not dramatically altered under the given nonlinearity condition. Effects of nonlinear interaction thus remained to be investigated under stronger conditions.

In this paper, we treat a straightforward procedure for loading atoms onto excited NBWs and solitons via the standing-wave pulse sequence in the bichromatic lattice. We consider the region where the interaction term does not go so far as to form the loop in the band structure. First, we analyze selection rules for transitions in the nonlinear system based on numerically obtained NBW bands. Since the NBWs are not orthogonal to each other, we numerically solve the time-dependent Gross-Pitaevskii equation (TD-GPE) to examine the selection rules. We will find that it is possible to load atoms onto soliton solutions in the periodic potential once appropriate parameters are obtained. Subsequently, we examine postloading effects of the external trapping harmonic potential and reveal that the dynamics reflect the nonlinear band dispersion. Finally, we discuss the dynamical instability using the method of linear stability analysis.

In passing, we note that the main observables in this paper are density distributions in position and momentum space, which are measurable in experiments. Besides fundamental techniques, our procedure requires only the control of the interaction strength that appears in the GPE. Furthermore, experimentally necessary parameters are taken from the papers of the Beijing group [20,26]; thus, this paper contributes to future experiments without any further complex coherent control.

The paper is organized as follows. Section II outlines the theoretical model system and shows nonlinear band dispersion. Section III discusses the selection rule of the loading process in terms of nonlinear Bloch waves. Section IV analyzes the numerical result of the loading process and postloading dynamics. Section V concludes the paper. Technical details are supplemented in the Appendixes.

II. MATHEMATICAL DEFINITION AND BASIC FEATURES OF THE SYSTEM

In the experimental papers of Refs. [19,20,26,27], the loading process begins with BEC in a three-dimensional (3D) harmonic trap. The dynamics is 3D and nonseparable since the interatomic interaction is in effect. However, here we consider the case where the harmonic confinement is much tighter in the y and z directions than in the x direction so that the system can be treated as quasi-one-dimensional (quasi-1D). Optimally parametrized 1D OL pulses are applied, and the momentum distributions of the postloading process are measured after the band mapping process.

Here, we solve the 1D TD-GPE [4] for interacting bosonic atoms in the bichromatic OL. Some notations and techniques used in this paper are available in our numerical studies presented in Refs. [24,28,29]. The TD-GPE reads

$$i\hbar\frac{d}{dt}\Psi(x') = \Bigg[-\frac{\hbar^2}{2m_a}\frac{\partial^2}{\partial x'^2} + \alpha(t)\{V_1\sin^2(k_r x') + V_2\sin^2(2k_r x')\} + \frac{1}{2}m_a\omega_0^2 x'^2 + g_{1D}N|\Psi(x')|^2\Bigg]\Psi(x'),$$

where V_1 is the height of the optical lattice with the period of $\lambda/2$, V_2 is with the period of $\lambda/4$, $\alpha(t)$ equals 1 during an on-duty cycle, otherwise it is zero, ω_0 is the frequency of the harmonic trap, N is the number of total atoms, and g_{1D} parametrizes the effective atom-atom interaction obtained by contracting the 3D trap to one dimension. We use recoil energy $E_r = \hbar^2 k_r^2/2m_a$ as the unit of energy, recoil momentum $k_r = 2\pi/\lambda$ as the unit of (quasi)momentum, lattice constant $\lambda/2$ as the unit of length, and rescaled time $t = E_r t'/\hbar$ as the unit of time. Here $\hbar$, λ, and m_a correspond to the Planck constant, the wavelength of the laser used for generating the OL, and the atomic mass, respectively. Rescaling the TD-GPE, we get

$$i\frac{d}{dt}\Psi(x) = \Bigg[-\frac{\partial^2}{\partial x^2} + \alpha(t)\{s_1\sin^2(x) + s_2\sin^2(2x)\} + \nu x^2 + g|\Psi(x)|^2\Bigg]\Psi(x), \tag{1}$$

where x, s_1, s_2, and g denote $x = k_r x'$, $s_1 = V_1/E_r$, $s_2 = V_2/E_r$, and $g = g_{1D}N/E_r$, respectively. The atom treated here is ^{87}Rb and typically g ranges from 10^{-5} to 1 [24,30]. The other parameters are the same as in Ref. [19]. We note that g could be made to take on any value by exploiting the Feshbach resonance [6]. We limit ourselves to the regime where $g \leqslant 8$ is comparable to the kinetic energy of the second excited band in this paper.

The nonlinear Bloch waves $\{\phi_{NB}(n, q, x)\}$ formed by the bichromatic OL alone satisfy the time-independent equation, namely,

$$\left\{-\frac{\partial^2}{\partial x^2} + s_1\sin^2(x) + s_2\sin^2(2x) + g_{\rm lat}|\phi_{NB}(n, q, x)|^2\right\} \times \phi_{NB}(n, q, x) = \mu\phi_{NB}(n, q, x) \tag{2}$$

subject to the normalization condition $\int_{-\pi/2}^{\pi/2}|\phi_{NB}(n, q, x)|^2 dx = \pi$. Here $g_{\rm lat}$ and μ correspond to the nonlinear interaction strength for NBWs and the chemical potential, respectively. The same as in the linear case [31], the NBW can be expanded as

$$\phi_{NB}(n, q, x) = e^{iqx}\sum_K C_{NB}(n, q, K)e^{2iKx}, \tag{3}$$

where q is the quasimomentum, $n \in \mathbb{N}$ is the band index, and $K \in \mathbb{Z}$ is the reciprocal vector index. From this, the coefficient

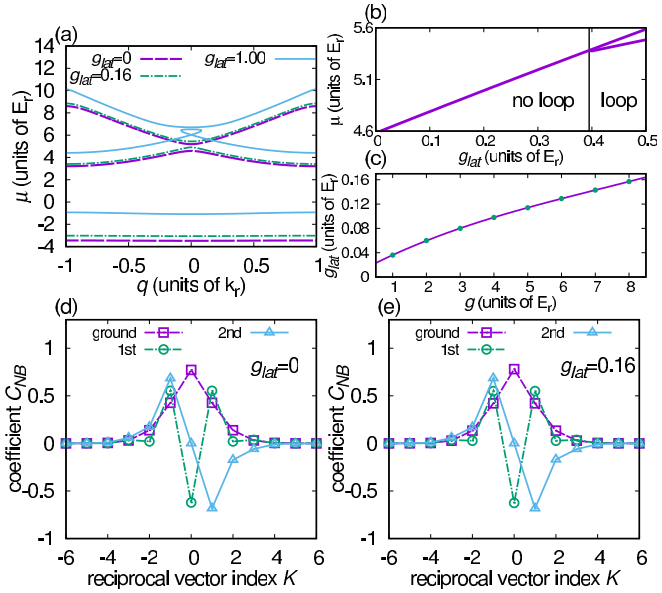

FIG. 1. (a) The band structure as a function of quasimomentum q for $g_{\rm lat} = 0$ (linear, purple dashed), $g_{\rm lat} = 0.16$ (green dash-dotted), and $g_{\rm lat} = 1$ (light blue solid) with $s_1 = 10$, $s_2 = 8$. Chemical potential is shown up to the second excited band. (b) The chemical potential μ of the nonlinear Bloch solutions as a function of interaction strength $g_{\rm lat}$ at $q = 0$ in the range $4.6 < \mu < 5.6$. If the interaction term is sufficiently small, only one eigenvalue appears for a given value of $g_{\rm lat}$ in this range. The loop appears at a point a little short of $g_{\rm lat} = 0.4$. (c) Numerically estimated interaction strength for the lattice system $g_{\rm lat}$ as a function of g. The green circles are the numerically obtained result, and the purple solid line is a fitted curve $g_{\rm lat} = 8.8 \times 10^{-3} + 2.9 \times 10^{-2} g - 2.2 \times 10^{-3} g^2 + 1.0 \times 10^{-4} g^3$. [(d), (e)] The first three Bloch coefficients as a function of K at $q = 0$ for $g_{\rm lat} = 0$ and 0.16, respectively. The odd excited and the even excited bands are pairwise inverted. Thus the first excited has even symmetry, and the seond has odd symmetry. In this region, the nonlinear interaction slightly alters the coefficients but does not modify the symmetry.

$C_{NB}(n, q, K)$ can be obtained by solving the nonlinear recurrent formula under the condition of $\sum_K |C_{NB}(n, q, K)|^2 = 1$ [4,5,13]. Figure 1(a) shows the first three band dispersions with $s_1 = 10$, $s_2 = 8$ with $g_{\rm lat} = 0$ (linear), 0.16, and 1. The trend of energy band dispersion is the same as a linear one if $g_{\rm lat} = 0.16$, except the interaction shifts the dispersion higher. Normally, the odd-excited band's coefficients have odd symmetry in K space and vice versa. However, the parity of the wave function of the first and second excited bands is inverted. Figures 1(d) and 1(e) show the coefficient $C_{NB}(n, q, K)$ of the first three bands at $q = 0$ with $g_{\rm lat} = 0$ and 0.16, respectively. In the linear limit, this parity inversion occurs with a change in the band structure: as s_2 increases, the gap between the first and second excited bands becomes smaller, and at the critical point $s_2 = (s_1/4)^2 = 6.25$, the gap disappears. For bigger s_2, the gap becomes larger and the parity of the wave functions of the first and second excited bands is inverted. See Ref. [24] for more detailed discussion.

Because the NBWs are not mutually orthogonal, nonzero overlap integrals occur between different momentum components of the target and unwanted states. Therefore, it appears to be worth examining the loading process numerically with TD-GPE. Furthermore, the nonlinear term is known to give rise to additional solutions other than usual Bloch solutions. One is the solution in momentum space corresponding to loop structures that appear at band edges. Figure 1(b) shows interaction strength dependency of the first excited band structure at $q = 0$. The interaction strength gradually modifies the structure, and the loop appears at around $g_{\rm lat} = 0.4$. For instance, we plotted a band structure with $g_{\rm lat} = 1$, which has a loop structure at $q = 0$ in the first excited band [Fig. 1(a)]. Typically, the top of the loop and the bottom of the second excited band become flat (see Appendix C for details). In addition to the NBWs, spatial soliton solutions having their chemical potential lying in a linear band gap are also allowed. These solutions are called the "gap soliton," consisting of NBWs with a hyperbolic-secant-type envelope typically. Therefore, this paper mainly aims to investigate how the loading process is affected by these additional solutions. See Refs. [4,5,13,32] for further detail about the loop structures and the solitons.

As seen in Eq. (2), $g_{\rm lat}$ corresponds to the nonlinear interaction at a specified single site; thus, the theory works perfectly if the wave function is thoroughly uniform (or perfectly periodic) over the whole spatial region. However, in our case, the simulation begins with the ground state of the harmonic system; therefore, the wave function is nonuniform and localized around the origin of the harmonic trap. Here we parametrize the interaction strength of the lattice system $g_{\rm lat} = g\bar{n}/\pi$ by averaged peak site density $\bar{n}$ after the loading process, where $\bar{n} = \int_{-\pi/2}^{\pi/2} |\Psi(x, \tau_{\rm total})|^2 dx$ and $\Psi(x, \tau_{\rm total})$ is the wave function immediately after the loading. This argument is the same as in the experimental paper done by Koller *et al.* [16]. Here, we use an equation obtained by a fitting for the relationship between g and $g_{\rm lat}$ under the condition of loading atoms onto the first excited band with $s_1 = 10$, $s_2 = 8$ [Fig. 1(c)]. This relationship is valid when $1 \leqslant g \leqslant 8$. For instance, in our numerical simulation, $g = 8$ corresponds to $g_{\rm lat} = 0.16$.

III. LOADING PROCESS

In the previous paper [24], we numerically optimized the loading process to the first and the second excited bands with a two-step on-off procedure in the linear limit as follows. We assumed that the atoms are initially installed in the ground state of the harmonic potential so that the initial state is an even symmetric zero-momentum state. Under this assumption, the time evolution during the on-duty cycle is given by the superposition of linear Bloch waves at $q = 0$. And the off-duty cycle changes the phase of the discretized momentum state. Thus, the net result can be regarded as a multipath interference effect in momentum space. With a grid spacing of 0.1 μs grid, we obtained through brute force the most appropriate time sequence $(\tau_1, \tau_1', \tau_2, \tau_2')$ for $q = 0$ with the total time $\tau_{\rm total} = \tau_1 + \tau_1' + \tau_2 + \tau_2'$ shorter than 100 μs. Here τ_n and τ_n' are the nth time durations for on- and off-duty cycles. According to the experimental paper of Ref. [19], the total time $\tau_{\rm total}$ is comparable to the scale of the recoil energy, since the unit of time in our definition $t = 1(\hbar/E_r)$ corresponds to 50.4 μs. To verify the availability of the protocol, subsequently, we applied the pulse-sequence method

TABLE I. Optimized loading protocols to the first and the second excited bands with two-step on-off procedure by using a brute force method with a period of 0.1 μs grid [24]. The lattice height is $s_1 = 10$, $s_2 = 8$. In this paper we chose the relative phase $\phi_{11} = \phi_{21} = \phi_{12} = \phi_{22} = \pi/4$ for antisymmetric loading for on-duty cycles. F is the fidelity of the optimization protocol in the linear limit. See Appendix A for more details.

Target	τ_1	τ_1'	τ_2	τ_2'	F
First excited, even	13.0	22.9	2.5	30.4	0.995
Second excited, odd	33.8	34.7	14.8	4.5	0.939

to a weakly interacting system ($g = 0 - 1$) by solving TD-GPE, starting with the ground state of the harmonic potential as before. Finally, we confirmed the protocols which were obtained in the linear limit were still valid for the weakly interacting system by calculating the density distribution after the band mapping process. In particular, in the previous paper [24], we focused on three sets of parameters in the symmetric (even-to-even) process, so that we had normal band structure ($s_1 = 10$, $s_2 = 5$), band structure with the Dirac-like point ($s_1 = 10$, $s_2 = 6.25$), and inverted band structure ($s_1 = 10$, $s_2 = 8$). This paper focuses on the inverted band structure, as shown in Fig. 1. Throughout this paper, we use the optimized protocol in the linear limit (Table I), although the nonlinear term takes place.

As seen in Eq. (1), a minimum of the OL term is set to coincide with that of the harmonic oscillator; that is, the pulse is symmetric under $x \to -x$. When this pulse acts on the zero-momentum initial state, which is symmetric, the solution evolves in time, maintaining the initial symmetry. On the other hand, loading atoms onto antisymmetric solutions requires an additional phase term in the OL pulse to break the symmetry of the initial state. Now consider that we apply the phase-shifted OL pulse to the system, namely,

$$s_1 \sin^2(x + \phi_{11}) + s_2 \sin^2(2\{x + \phi_{21}\})$$

for the first on-duty cycle, and

$$s_1 \sin^2(x + \phi_{12}) + s_2 \sin^2(2\{x + \phi_{22}\})$$

for the second one. Indeed, the Fourier coefficients of the OL other than the constant term $\frac{s_1+s_2}{2}$ are essential in the discussion of symmetry. If, for example, $\phi_{11} = \phi_{21} = \pi/4$ and $\phi_{12} = \phi_{22} = \pi/8$, the OL becomes antisymmetric under $x \to -x$ as can be seen by shifting the OL potential by a constant $\frac{s_1+s_2}{2}$. However, here we simply consider $\phi_{11} = \phi_{21} = \phi_{12} = \phi_{22} = \pi/4$ for experimental implementation although the pulse is only partially antisymmetric. See Appendix A for the details about the effect of relative phases. Let us consider the reachable target state with the antisymmetric loading process at $q = 0$ in the linear limit. When the lattice height s_2 is lower than the critical value $(s_1/4)^2$, the linear Bloch wave at $q = 0$ of the first excited band has odd symmetry in K space, and the second has even. Therefore, the antisymmetric loading process fails to load atoms onto the second excited band. Once s_2 exceeds $(s_1/4)^2$, the parity of the linear Bloch waves in K space is inverted [Fig. 1(d)], so the atoms cannot be loaded onto the first excited band with the antisymmetric loading process.

In K space, the first excited band solution with $g_{\rm lat} = 0.16$ behaves almost the same as the linear one (see Fig. 1). Therefore, even when the effect of the nonlinear term becomes a little stronger in this case, we try loading the atoms using the same time sequence as in the linear case shown in Table I. Let us note that unlike the linear case, the time evolution cannot be described by an expansion over eigenstates in the nonlinear case. Therefore, we applied the fourth-order split-step Fourier method for time propagation [33]. When the interaction strength is strong enough, a new NBW solution emerges, which corresponds to the loop structure. In addition to this interesting phenomenon, there appears another nontrivial set of spatial solutions called "solitons." The main focus of this paper is to present a method to load atoms onto NBWs and also onto soliton solutions. We then discuss the stability of the solitons after the loading.

IV. DISCUSSIONS ON NUMERICAL RESULTS

This section discusses the numerical result of the loading process with the inverted band structure ($s_1 = 10$, $s_2 = 8$) for the interaction strength $g = 1$-8. In the previous experiments [20,21], the loading efficiency is estimated by observing the postloading dynamics of the atoms by suddenly freezing the OL in time. The Faraday imaging method can directly observe the motion of atoms in position space with sufficiently high resolution [34]. We note that, in our parameter regime, single-site resolved imaging is not necessary to observe the dynamics of wave packets since the wave packets are spatially spread over several sites. Observing wave packets with single-site resolved imaging would help understand more detailed dynamics and structures of the solitons. As for the experimental techniques of single-site resolved imaging, refer to Refs. [35,36] and references therein. The band mapping technique is one of the most promising experimental methods that maps the quasimomentum of the loaded atoms onto the real momentum domain and reveals the band indices [37–39]. Therefore, we analyze the density distribution in momentum space as well as in position space, which is obtained by the band mapping procedure, in order to study the postloading dynamics. For the numerical implementation, we chose 1.0 ms for the whole band mapping process with a decay constant $\gamma = 500$ μs according to Ref. [20].

First, we discuss the postloading dynamics with only the OL on (case 1). We show that the loading process can load atoms onto soliton solutions if the interaction strength is high enough. Second, we study the case when the harmonic potential is added, and discuss how the wave packet behaves under the influence of the harmonic trap (case 2). Finally, we study the postloading dynamics when the initial state is not a clean ground state but affected by an artificial noise. And we discuss the effect of dynamical instabilities (case 3). In all the cases listed above, the numerical simulation begins with the ground state $\psi(x)$ in the harmonic trap with $\nu = 1.2 \times 10^{-4}$ (corresponding to $2\pi \times 70$ Hz) at a certain interaction strength g. And in case 3, we use the ground state

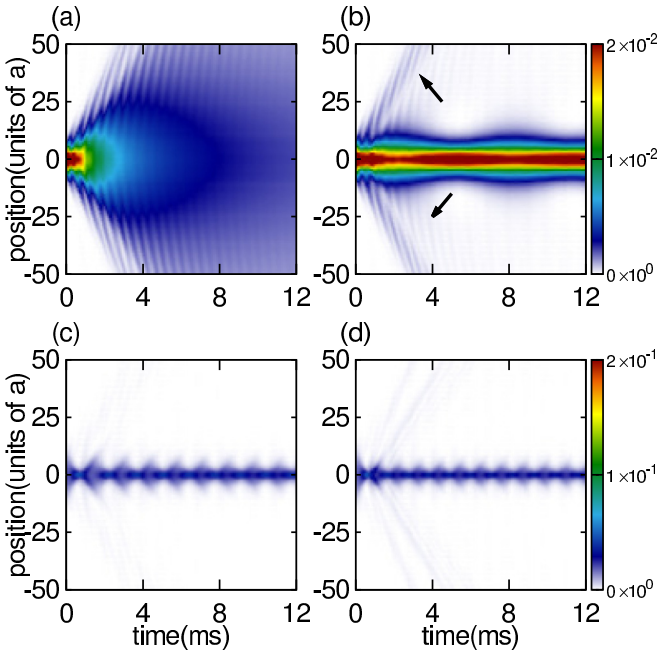

FIG. 2. Time evolution of the wave packet in position space as a function of holding time with $s_2 = 8$ for (a) $g = 1$, (b) $g = 2$, (c) $g = 4$ and (d) $g = 8$. In (a), the wave packet spreads out over time due to the tunneling. When the interaction strength becomes $g \geqslant 2$, the atoms are loaded to soliton states, and most of the wave packets localize at the origin of the initial state over time. As the interaction strength g becomes stronger, the frequency of the breathing mode increases and the width of the soliton decreases. The visible expanding components (faint blue line and black arrow) mainly consist of first excited band component in (b). Similar components appear in (c) and (d), although the density is lower.

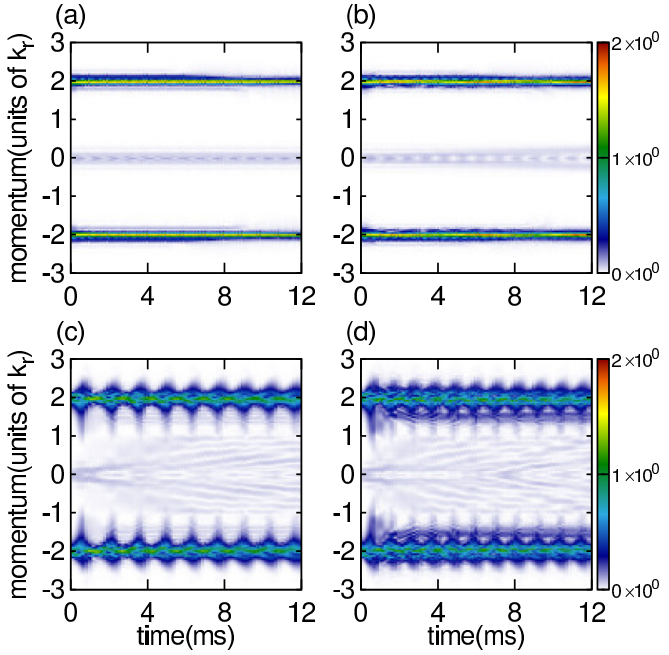

FIG. 3. Time evolution of the wave packet in momentum space after the band mapping process as a function of holding time with $s_2 = 8$ for (a) $g = 1$, (b) $g = 2$, (c) $g = 4$, and (d) $g = 8$. In all cases, the wave packet is located at around $p = 2$. In (c) and (d), the oscillation of the breathing mode can be seen clearly.

$\psi(x)$ with additional artificial Gaussian noise as the initial state to simulate TD-GPE.

A. Case 1: Postloading dynamics with only OL

The mean momentum of the initial wave function is zero, and its width in momentum space is around $0.1k_r$. The loading process essentially preserves quasimomentum since the time required for the loading is short enough. Therefore, the loaded atoms can appear throughout many bands, but only around $q = 0$. If there is no interaction and if there is no external potential other than OL, the atoms loaded in a particular band spread out on the time scale deriving from the tunneling term. The dynamics is described by the superposition of various Bloch states around $q = 0$ in a specific band, so that the interference of these closely located states leads to the appearance of fringes. The interference pattern depends on the dispersion of the loaded band. In other words, measuring the postloading dynamics with OL allows us to analyze the band dispersion around $q = 0$. Examination of this issue is interesting, particularly in the presence of the Dirac point [24,40,41], but we present this case in a separate article.

In this section, we examine the effect of the interaction term on the postloading dynamics. Here, we apply the two-step duty cycle shown in Table I, and then turn on only the OL and keep it on after the loading process. Figure 2 shows the dynamics of the loaded atoms in position space after the loading to the symmetric solution of the first excited band (even to even). And the corresponding momentum distribution after the band mapping process is shown for various cases in Fig. 3. When the interaction strength is weak enough [$g = 1$ in Fig. 3(a)], the postloading dynamics directly reflects the local nonlinear band dispersion as shown in Fig. 1. In position space, the wave packet spreads out over time centered at the origin of the initial state while the momentum distribution [Fig. 3(a)] is localized at $|p| = 2$. Above $g = 2$, the dynamics shows solitonic behavior. The wave packet is localized around the origin of the initial state and shows a breathing oscillation [12,42] in position space without significant spreading [Figs. 2(b)–2(d)]. On the other hand, in momentum space, it remains almost unchanged, and the atoms are localized around $|p| = 2$ [Figs. 3(b)–3(d)]. In terms of band dispersion, an immobile wave packet corresponds to a flatlike dispersion. The loop top dispersion becomes flatlike if the interaction strength is high enough ($g_{\mathrm{lat}} \geqslant 0.4$). However, even without such shape deformation of the band dispersion, localized wave packets appear [see Fig. 2(b): $g_{\mathrm{lat}} = 0.06$]. The results suggest that the localization of the wave packet is not merely due to the band dispersion but to the appearance of soliton solutions. We also evaluate the loading rate around $p = |m|(m \in \mathbb{N})$ by integrating the wave function in the momentum space, $R_m = (\int_{m-0.5}^{m+0.5} |\psi(p)|^2 dp + \int_{-m-0.5}^{-m+0.5} |\psi(p)|^2 dp) / \int_{-\infty}^{\infty} |\psi(p)|^2 dp$. Here $\psi(p)$ is obtained by applying the band mapping procedure to the wave function immediately after the loading, $\psi(x, \tau_{\mathrm{total}})$. For $m = 0$, the range of integration is simply $p = -0.5$ to 0.5. Table II shows the results for $g = 1$, 2, 4, and 8. We note that the loading

TABLE II. The loading rate R_m with $g = 1$, 2, 4, and 8. In all cases, R_1 and R_3 are always smaller than 10^{-3}. R_2 is about 10% smaller than the optimized fidelity F in the linear limit.

	$g=1$	$g=2$	$g=4$	$g=8$
R_0	0.031	0.062	0.037	0.037
R_2	0.855	0.929	0.876	0.888
R_4	0.058	0.004	0.042	0.032

rate is just the population around the mth band edge. In order to estimate the band population more precisely, the wave packet must be moved far enough away from the band edges. Due to the nontrivial nonlinear interaction, the relationship between the loading rate and the interaction strength cannot be expressed by a monotonic function.

In order to show the solitons more clearly, we plotted the density profile after the loading process in Fig. 4. Figures 4(a) and 4(c) show density profiles immediately after the loading for $g = 2$ and 8. A Gaussian shape approximately describes the profile since the loading process is not long enough to modify the envelope. After the 10-ms holding time, the nonsoliton component goes far enough away from the origin of the initial state, and the immobile component remains at $x = 0$. Then the envelope of the wave packet becomes hyperbolic secant [Figs. 4(b) and 4(d)], which is one of the characteristic behaviors of solitons. In addition to that, in a smaller structure, the wave functions have two nodes per site [Figs. 4(c) and 4(f)]. This structure suggests that the soliton solutions are attributed to the NBWs in the first excited band. We estimated the averaged chemical potential as $\langle\mu(t)\rangle = \int_{x_l}^{x_u} \psi(x,t)^* \mu \psi(x,t) dx / \int_{x_l}^{x_u} \psi(x,t)^* \psi(x,t) dx$. We chose $x_l = -20\pi$ and $x_u = 20\pi$ for numerical convergence. The chemical potential oscillates as a function of time since the wave packet is in breathing mode. Therefore, we show the minimum value of the averaged chemical potential between 8 and 12 ms, $\langle\mu\rangle_{\min}$, in Table III. The averaged chemical potential is slightly lower than the chemical potential, which is estimated by the mean density immediately after the loading process. However, the chemical potential lies between the first and second excited linear band gap ($4.58 \leqslant \mu \leqslant 5.19$), although it is difficult to identify the soliton solution exactly. We also showed $P_{\rm sol}(t) = \int_{x_l}^{x_u} |\psi(x,t)|^2 dx$ to estimate the population of the soliton at $t = 12$ ms. As the interaction becomes

TABLE III. Relationship between the interaction strength g and the chemical potential of the solitons, $\langle\mu\rangle_{\min}$. The chemical potential $\mu(q=0)$ of the first excited band at $q = 0$ is obtained by Figs. 1(b) and 1(c). The wave function of the central site immediately after the loading has a high density because of the extra components. $\mu(q=0)$ is always higher than $\langle\mu\rangle_{\min}$. We numerically estimated the soliton population $P_{\rm sol}$ at $t = 12$ ms for future experiments. See text for more detail.

g	$\mu(q=0)$	$\langle\mu\rangle_{\min}$	$P_{\rm sol}$
2	4.71	4.61	0.902
4	4.78	4.68	0.878
6	4.85	4.74	0.819
8	4.90	4.79	0.705

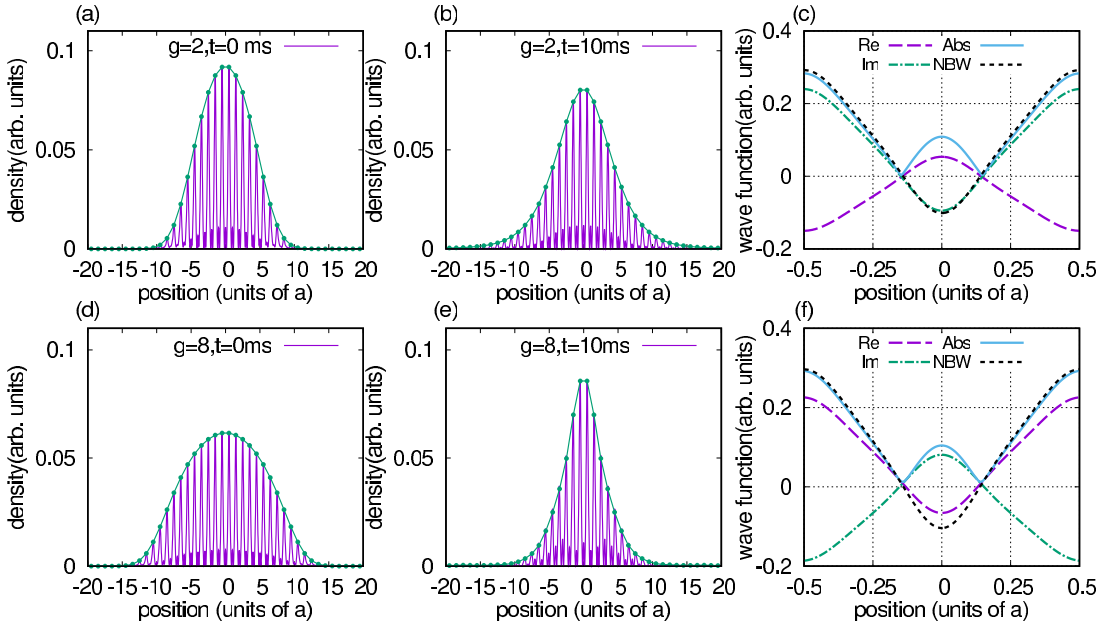

FIG. 4. The density profile immediately after the loading process for (a) $g = 2$ and (c) $g = 8$. Purple and green lines correspond to the density profile and envelope function in position space, respectively. The envelopes are well fitted by the Gaussian function, reflecting the initial state. (b) and (e) correspond to the density profile after 10 ms holding with $g = 2$ and $g = 8$, respectively. The nonsoliton component goes away from the origin; thus, only the soliton solution remains around $x = 0$. The corresponding envelopes are hyperbolic secant in both cases. (c) and (f) are enlarged views of the central site $-0.5 \leqslant x \leqslant 0.5$ of (b) and (e), respectively. Purple long-dashed, green dash-dotted, and light blue solid curves correspond to the real part, imaginary part, and absolute value of the wave function, respectively. The black dashed lines indicate the NBW $\phi_{NB}(1, 0, x)$ of the first excited band at $q = 0$ with (c) $g_{\rm lat} = 0.06$ and (f) 0.16.

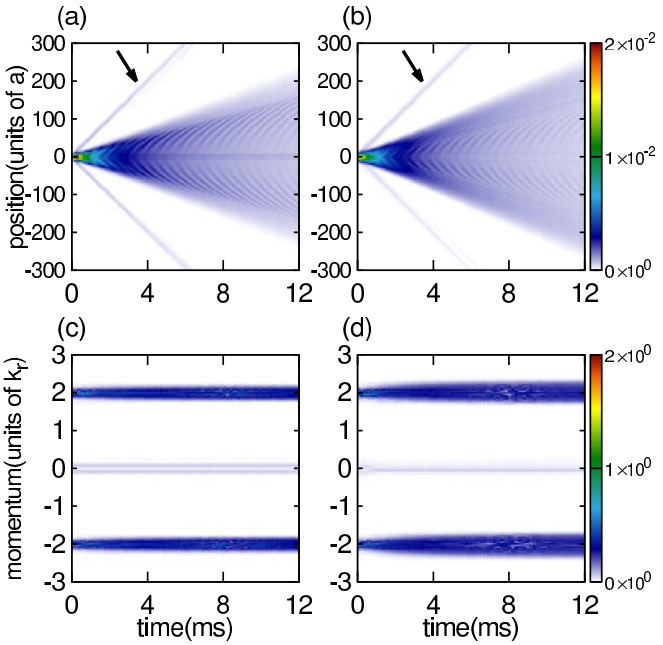

FIG. 5. Time evolution of the wave packet in (a, b) position space and (c, d) momentum space with the protocol for loading atoms onto antisymmetric solutions. Here the target state is the bottom of the second excited band. (a) and (c) corresponding to the weakly interacting case with $g = 1$. (b) and (d) corresponding to the strongly interacting case with $g = 8$. The interaction strength does not drastically alter the trends. In both cases, fast-moving wave packets appear in position space (black arrow). These wave packets consist of fourth excited band components, unlike the symmetric loading case (Fig. 2).

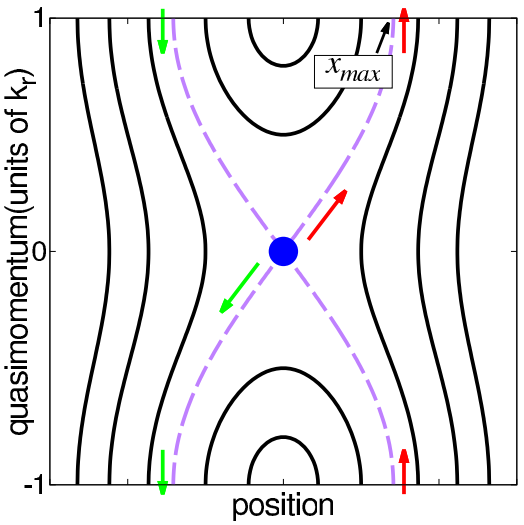

FIG. 6. Typical isoenergetic surface of the first excited band with the reduced zone representation. The surface is given by the one-dimensional classical pendulum H_{cl}. The purple dashed line and the blue circle correspond to a separatrix and a rough coordinate of the atoms immediately after the loading. In our case, the atoms are loaded onto the origin of the surface, then half of the wave packet moves up along the separatrix lines (red arrow), and the rest moves down (green arrow). Due to the Bragg reflection, the quasimomentum of the wave packet is reversed when they reach the band edge.

stronger, the population of the soliton decreases. The details of the soliton solution in the bichromatic OL system, such as spectrum and the fundamental gap soliton, are interesting, but the discussion is beyond the scope of this paper. In passing, we note that it is difficult to generate specific solitons or to specify soliton modes at this stage since the final state is sensitive to the initial state, time sequence, and so on.

We also examined the loading process to the bottom of the second excited band (even to odd) with $s_1 = 10$, $s_2 = 8$. Figures 5(a) and 5(b) show the time evolution of the wave packet with $g = 1$ and 8, respectively. In position space, the loaded atoms spread out over time, the same as in Fig. 2(a). As seen in Fig. 1(c), the second excited bands are not strongly deformed by the interaction, and the gap appears around $|q| = 1$. Therefore, in contrast to the previous case, the postloading dynamics behave as in the linear case (or weakly interacting case) even when the interaction is strong ($g = 8$). The momentum distribution shows that most of the atoms appear around $|p| = 2$, which means the protocol successfully loaded atoms onto the bottom of the second excited band. We note that, as discussed in Ref. [21], the OL pulses with nonzero relative phases $\phi_{11} = \phi_{21} = \phi_{12} = \phi_{22} \neq 0$ reduce the loading efficiency; small portions are loaded onto the ground and the fourth excited band. Table IV shows the loading rate R_m. In both cases, 15% of atoms are loaded onto the fourth band edge. In order to achieve higher loading efficiency, an optimization based on TD-GPE would be necessary.

TABLE IV. The loading rate R_m with $g = 1$ and 8 (same as Table II). R_1, R_3 are always smaller than 10^{-3}.

	$g = 1$	$g = 8$
R_0	0.050	0.050
R_2	0.714	0.748
R_4	0.179	0.152

In passing, we note that we have examined the loading process with a standard band of $s_1 = 10$, $s_2 = 5$. In this case, the atoms are loaded onto the soliton solution between the first and second excited bands with the antisymmetric (even-to-odd) loading protocol. Appendix B discusses more details of the results with the normal band. We also note that our procedure is valid in the limit of the monochromatic lattice, e.g., $s_1 = 10$, $s_2 = 0$ (standard band). Although antisymmetric loading is required for soliton generation, the experimental implementation may be simpler than the bichromatic system. The loading process with the Dirac-like point is of sufficient interest that it will be studied separately elsewhere.

B. Case 2: Postexcitation dynamics with harmonic OL

In the ultracold atomic system, time modulation of the optical lattice and time variation of the external potential can be experimentally realized [43]. Band spectroscopy of the atoms in OL is one of the essential applications. By combining linear potentials with OL, a Stückelberg-type interferometer can be constructed and measured by observing momentum distributions [44]. Dispersions can also be measured by modulating the height of the optical lattice in time to inducing

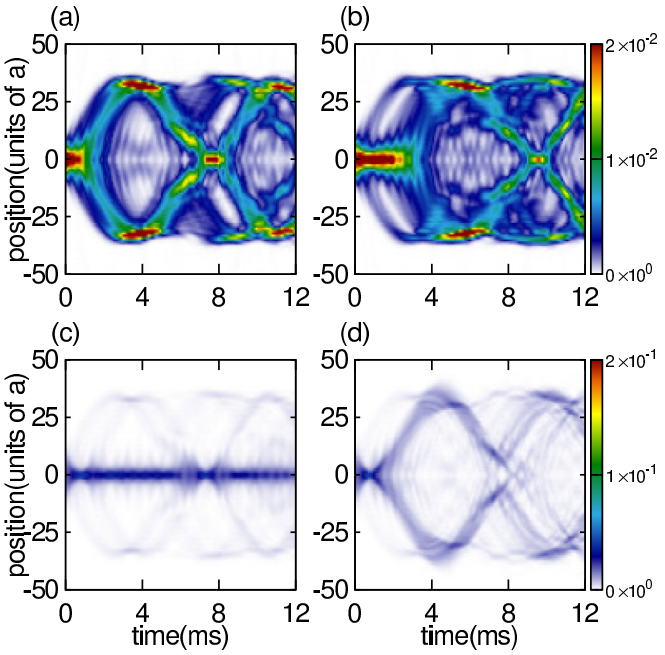

FIG. 7. Time evolution of the wave packet in position space as a function of holding time with $s_2 = 8$ for (a) $g = 2$, (b) $g = 4$, (c) $g = 6$, and (d) $g = 8$. Atoms are initially loaded to soliton solutions and the soliton decays to the first excited band after a certain holding time. The atoms follow the isoenergetic surface of the one-dimensional classical pendulum given by H_{cl} (see Fig. 6).

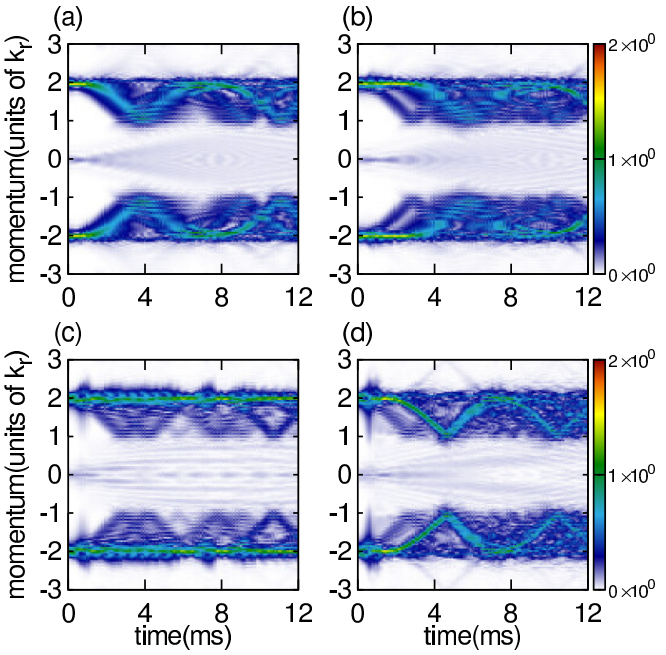

FIG. 8. Time evolution of the wave packet in momentum space after the band mapping process as a function of holding time with $s_2 = 8$ for (a) $g = 2$, (b) $g = 4$, (c) $g = 6$, and (d) $g = 8$ corresponding to Fig. 7.

interband transitions [45]. The Aarhus group experimentally measured the spectrum formed by the combined potential of the OL and the harmonic potential by using amplitude modulation of the OL with the acceleration of atoms due to the harmonic potential [46]. Thus, the observation of the dynamics of atoms in the combined potential of the OL and the external potential is important for further applications. Here we discuss the dynamics of loaded atoms with strong nonlinearity under the influence of the harmonic trap to identify global band dispersion and stability. From the viewpoint of the classical interpretation under the single-band approximation, the dynamics is simply given by $H_{cl}(q, x) = \mu(q) + \nu x^2$ [38]. Figure 6 shows a typical isoenergetic surface of the first excited band in the linear limit ($g = 0$) with a reduced zone representation. The dispersion can be treated as a cosine function under the first-order tight-binding approximation in the linear limit. Therefore, a trajectory of the loaded atoms traces a classical pendulum [24,28,47]. If the atoms are loaded on the origin of the surface, the atoms follow a line of the separatrix. According to H_{cl}, we can easily estimate the maximum position of the atoms, $x_{\max}$. In the case of $s_1 = 10$, $s_2 = 8$, and $\nu = 1.2 \times 10^{-4}$, $x_{\max} \simeq 33$ sites (see Refs. [24,28] for details). Since the small nonlinear interaction does not alter the band dispersion drastically, the classical interpretation may work even with the nonlinear term $g \leqslant 8$. Thus, measuring postloading dynamics allows us to compute a general form of the band where the atoms are loaded.

Figure 7 shows the postloading dynamics of the symmetric process with harmonic trap for $s_1 = 10$, $s_2 = 8$ with $\nu = 1.2 \times 10^{-4}$. Figure 8 shows corresponding momentum distributions after the band mapping process. As shown in Fig. 2, the process loads atoms to the soliton solution in $g = 2$-8. The acceleration force due to the harmonic potential lowers the density of the soliton so that the loaded atoms decay to the first excited band from the soliton solution after a certain holding time. In terms of the tight-binding approach, the harmonic potential modifies the spatially uniform tunneling constant to nonuniform. Therefore, in the presence of the harmonic trap, the soliton solution of the uniform lattice is not stable anymore. As the interaction strength increases, the soliton gets more stable up to $g = 6$ which corresponds to $g_{\text{lat}} = 0.13$ [see Fig. 1(b)]. When the interaction strength reaches $g = 8$, the soliton decays immediately after the loading. To confirm this effect more clearly, we also plot a scaled autocorrelation function

$$A(t) = |\langle \Psi(t = \tau_{\text{total}})|\Psi(t)\rangle|^2 / |\langle \Psi(t = \tau_{\text{total}})| \times \Psi(t = \tau_{\text{total}})\rangle|^2$$

as a function of the holding time in Figs. 9(a) and 9(b) with $\nu = 1.2 \times 10^{-4}$ and $\nu = 2.5 \times 10^{-4}$, respectively. $\Psi(t = \tau_{\text{total}})$ is a wave function immediately after the loading process. In Fig. 9(a), the autocorrelation function is most stable at $g = 6$. In the other cases, the autocorrelation functions quickly become unstable, then show revival due to the classical orbit given by H_{cl}. We note that this phenomenon depends on the balance between the nonlinear term and the strength of the harmonic trap. In the case with $\nu = 2.5 \times 10^{-4}$ [Fig. 9(b)], the autocorrelation function shows higher stability for $g = 8$ than for $g = 6$. The effects due to the external potentials are interesting because they are related to manipulating solitons in the coordinate space, but we leave it out of this paper.

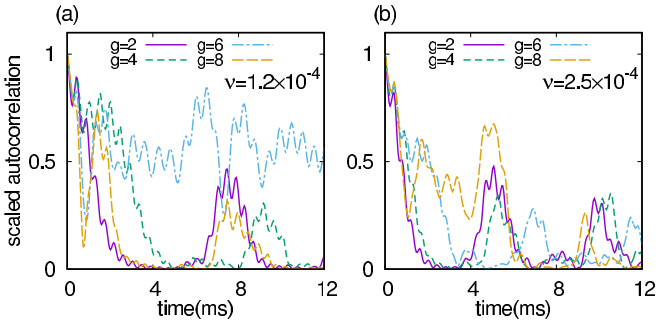

FIG. 9. Autocorrelation function $A(t)$ as a function of holding time with (a) $\nu = 1.2 \times 10^{-4}$ and (b) $\nu = 2.5 \times 10^{-4}$. Purple solid, green dashed, light blue dash-dotted, and orange long-dashed curves correspond to $g = 2, 4, 6$, and 8, respectively. (a) In the case of $g = 6$, the autocorrelation shows a stable feature. In other cases, the soliton decays within 4 ms; subsequently, it shows revivals due to the closed classical trajectories given by H_{cl}. (b) In the case of $\nu = 2.5 \times 10^{-4}$, $g = 8$ is most stable. See text for more detail.

C. Case 3: Effect of instability

One of the unique features of the lattice BEC system is dynamical instability. This instability is considered a counterpart of an energetic instability and causes NBWs (solitons) to be unstable when additional perturbative modes exist. To explore dynamical instability of NBWs, we follow the discussion in Refs. [4,5]. We assume that NBWs experience a small perturbation with momentum f as $\psi = \phi_{NB}(n, q, x) + \delta\psi$, where $\delta\psi = e^{iqx}\{u_f(x)e^{ifx} + v_f^*(x)e^{-ifx}\}$.

The perturbative part $\delta\psi$ obeys the time-dependent equation

$$\frac{d}{dt}\begin{pmatrix} u_f \\ v_f \end{pmatrix} = \hat{\sigma}_z\hat{B}\begin{pmatrix} u_f \\ v_f \end{pmatrix} = \Lambda_l(q)\begin{pmatrix} u_f \\ v_f \end{pmatrix}, \tag{4}$$

where the operator

$$\hat{B} = \begin{pmatrix} L_+ & g_{\rm lat}\Phi^2(n,q) \\ g_{\rm lat}\{\Phi^*(n,q)\}^2 & L_- \end{pmatrix} \tag{5}$$

and diagonal part

$$L_\pm = -\left[\frac{d}{dx} + i(\pm q + f)\right]^2 + s_1\sin^2(x) + s_2\sin^2(2x) - \mu + 2g_{\rm lat}|\phi_{NB}(n,q,x)|^2 \tag{6}$$

with Pauli matrix $\hat{\sigma}_z = \left(\begin{smallmatrix} 1 & 0 \\ 0 & -1 \end{smallmatrix}\right)$ and $\Phi(n,q) = e^{-iqx}\phi_{NB}(n,q,x)$. Here the operator $\hat{\sigma}_z\hat{B}$ is non-Hermitian; thus, eigenvalues $\Lambda_l(q)$ can be complex. Besides, complex eigenvalues always appear in pairs: one has a positive imaginary part, and the other has a negative. Therefore, if the operator $\hat{\sigma}_z\hat{B}$ has complex eigenvalues, the state grows exponentially in time.

Figure 10 shows the maximum absolute values of the imaginary part of the eigenvalues $\mathrm{Im}\Lambda_l(q)$ of the first excited band at $q = 0$. A strongly unstable regime appears around $q = 0$. The result implies that the soliton solutions containing NBWs of the first excited band at $q = 0$ are unstable, according to the composite relation [13]. While features of dynamical instability cannot be clearly seen within 12 ms postloading

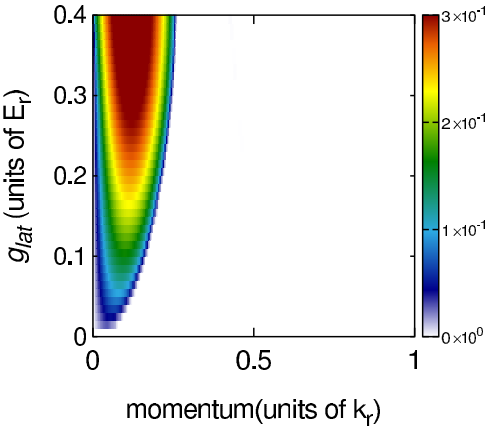

FIG. 10. The maximum absolute values of the imaginary part of the eigenvalues $\mathrm{Im}\Lambda_l(q)$ for the first excited band. The unit of the color bar is E_r. The vertical axis corresponds to interaction strength $g_{\rm lat}$ and the horizontal to perturbative momentum f. Values become higher toward red and lower toward white. White corresponds to a dynamically stable regime. The unstable regime appears around $f = 0$.

dynamics in the previous section, dynamical instability may break the stable wave packet for long-term propagation.

In order to investigate dynamical instability more deeply, we numerically solved the TD-GPE with an artificial Gaussian-type noise in addition to the condensate initial function $\Psi(t = 0, x) = \psi(x) + \Delta(x)$ (see Ref. [48]), namely,

$$\Delta(x) = \epsilon\psi(x = 0)r(x)e^{-x^2/\sigma^2}, \tag{7}$$

where $\psi(x = 0)$ is the BEC in the harmonic potential and $r(x)$ is a random number uniformly distributed in [0,1]. We chose $\epsilon = 0.1$ and $\sigma = 20\pi$. Figure 11 shows the density profile after the loading process as a function of holding time in position space with $s_2 = 8$. Only the OL is turned on while the holding process. In Figs. 11(a) and 11(b), dynamical instability does not strongly break the symmetry within 12 ms, although the imaginary part appears around $f = 0$. The absolute value of the imaginary part increases as it increases the interaction strength to $g = 6$; the effect of dynamical instability can be seen clearly in the density profile. We also plot the scaled autocorrelation $A(t)$ as a function of holding time in Fig. 12. In the case of $g = 2$, the noise makes the autocorrelation stable since it suppresses a coherence of the breathing mode. We note that the random noise might correspond to experimental imperfections, e.g., an unspecifiable excited state; however, this analysis is more of a numerical check. The shape of the noise function may be spatially correlated, and the random noise may be totally different from the real experimental environment. It is required to know the sources of the noises more precisely to investigate the environmental effect.

V. CONCLUSIONS

We discussed the standing-wave pulse sequence [19,21] in the one-dimensional bichromatic system with atom-atom interaction in terms of mean-field theory. In the previous paper [24], we showed that the pulse sequence is essentially multipath interference in the momentum domain. And the parity

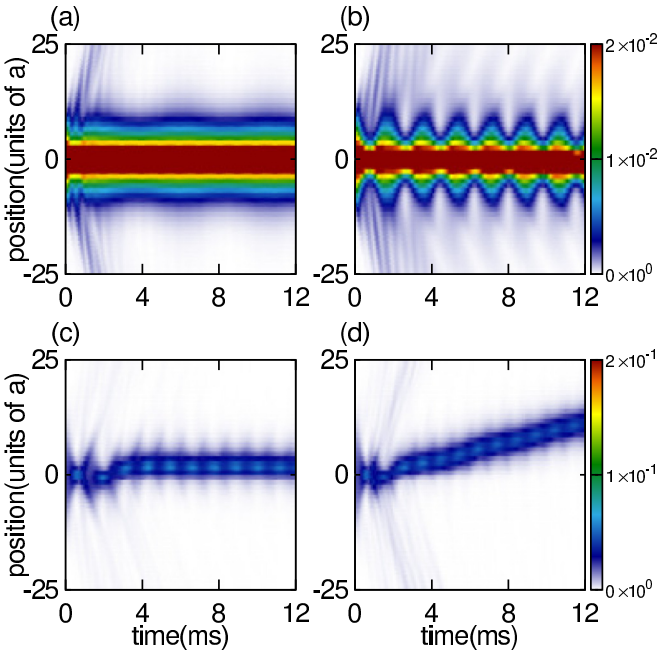

FIG. 11. Postloading dynamics with a Gaussian noise for $s_1 = 10$, $s_2 = 8$. For (a) $g = 2$ and (b) $g = 4$, the dynamics is stable despite the noise is added. On the contrary, for (c) $g = 6$ and (d) $g = 8$, the symmetry of the wave packet is broken due to the noise.

selection rule of the pulse sequence is specified by the orthonormal Bloch solutions in the linear case. We also verified that the weak nonlinearity $g < 1$ does not alter the results dramatically. In this paper, we extended our theoretical work [24] to the strongly nonlinear regime. Contrary to the linear case, the NBWs are nonorthonormal, and additional loop structures appear at the band edges in the time-independent spectrum. In addition to that, the spatially localized soliton solutions appear, which are connected to NBWs through a composite relation [13]. Therefore, the loading process to NBWs is a nontrivial issue.

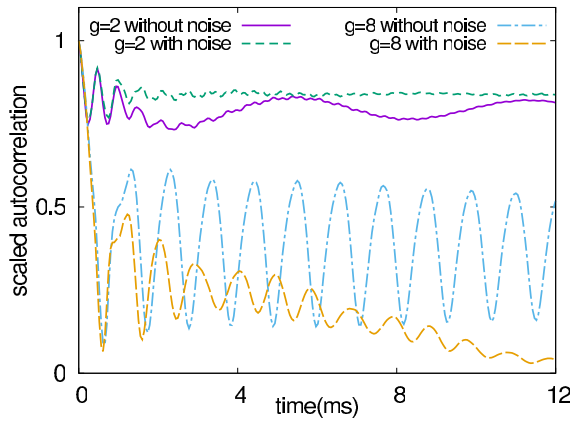

FIG. 12. Autocorrelation function $A(t)$ as a function of holding time. Green dashed (orange long-dashed) and purple solid (light blue dash-dotted) curves correspond to $g = 2$ ($g = 8$) with and without noise.

In order to examine the loading process to NBWs, we numerically simulated the pulse sequence with the inverted band. We found that the sequence can load atoms to the soliton solution in the excited band with an appropriate time interval of the pulses when the interaction strength is high enough. And we numerically verified that the sequence is valid up to $g = 8$. The postloading dynamics with only OL show that the nonsoliton components quickly move away, leaving the soliton solution at the initial position of the wave packet. In the periodic potential, the soliton component stays in its initial position and oscillates in the breathing mode according to the interaction strength. Subsequently, we showed the postloading dynamics with the addition of an external harmonic potential to check the solitons' stability. The harmonic potential modulates the tunneling constant; thus, the soliton decays after a certain holding time. Finally, we discussed the effect of the dynamical instability in terms of the linear stability analysis [4,5]. The spectrum of the time propagation operator shows that the nonlinear Bloch solutions are unstable at $q = 0$. In order to verify the dynamical instability, we numerically simulated noise by solving the TD-GPE using an artificial noise function mixed into the BEC's initial state and found that the process nevertheless succeeded in loading atoms to the soliton solution. However, the noise suppresses coherence of the breathing oscillation and leads to instability while holding. Our theoretical analysis recommends the range of interaction strength $g = 2$-6 for future experiments. This paper showed how to load atoms onto soliton solutions with the periodic potential. The obtained soliton solutions are in the breathing mode with a hyperbolic-secant-type envelope. The soliton solution has a complex spectrum that depends on many parameters [12,13]. Therefore, the manipulation of the modes and the envelopes of solitons are expected to be difficult in the method of this paper. Reinforcement learning using the nonlinear GPE will be more appropriate than the brute force method with the linear Bloch equation.

Compared to the adiabatic process, the standing-wave pulse method can load atoms in a shorter period of time [19,21]. Moreover, compared to the other methods [49], it only requires controlling time intervals of lattice pulse with a precision of 0.1 μs. However, there is still much to be explored from the theoretical point of view in the field of ultracold atomic physics. For example, Ref. [16] reports that there may be additional instability due to the beyond-mean-field correlation. The theoretical paper in Ref. [50] considers fouth-order interaction proportional to $|\Psi|^4$ in the case of a strongly interacting limit. A recent paper [18] took into account additional terms corresponding to third-order correction ($\propto g_3$) and the three-body loss rate ($\propto K_3$) given in the form of $g_3|\Psi|^3 - iK_3|\Psi|^4$ which is called the Lee-Huang-Yang term.

As for future applications in ultracold atomic physics, combinations of standing-wave pulse sequence and the other experimental techniques would lead to a powerful strategy for coherent manipulation of the nonlinear wave packets. The amplitude modulation leads to coherent band couplings, which allow us to produce modified band structures with vast Hilbert space [51,52]. In this paper, we applied the external harmonic potential for inducing intraband transition as a very practical example. Indeed, there are many other methods to induce intraband transition. As an example, a phase

modulation technique such as the topological pumping process [53] would lead to unique coherent manipulations. In addition to manipulations on the center-of-mass motion, manipulations on the internal degrees of freedom should be able to open up insights into designing new quantum devices. In particular, the multicomponent system would be a very nice platform. The appropriate combinations of the coherent control may produce gap solitons with spin-orbit coupling [54], stabilized NBWs [55], and so forth. Much remains to be studied.

ACKNOWLEDGMENT

T.Y. acknowledges support from JSPS KAKENHI Grant No. JP20K15190.

APPENDIX A: OPTIMIZED TIME INTERVAL FOR PULSE SEQUENCE

The linear Bloch waves are given in the same formula as $\phi_B(n,q,x)=\sum_K C_B(n,q,K)e^{2iKx}$ which are the eigensolutions of the time-independent Bloch Hamiltonian $H_B=-\frac{d^2}{dx^2}+s_1\sin^2(x+\phi_1)+s_2\sin^2(2\{x+\phi_2\})$. Here ϕ_1 and ϕ_2 are controllable phases for the OL. The Bloch coefficients $C_B(n,K,q)$ can be obtained by solving the recurrent formula

$$\begin{aligned}&(q+2K)^2C_B(n,q,K)-s_2e^{-4i\phi_2}C_B(n,q,K-2)/4\\&\quad-s_1e^{-2i\phi_1}C_B(n,q,K-1)/4-s_1e^{2i\phi_1}C_B(n,q,K+1)/4\\&\quad-s_2e^{4i\phi_2}C_B(n,q,K+2)/4\\&=\big(E_q^n-s_1/2-s_2/2\big)C_B(n,q,K),\end{aligned}\tag{A1}$$

namely, the central equation (see Ref. [31] and our previous work [24]), where E_q^n represents the eigenenergy of the Bloch state.

In the linear regime, once the Bloch waves are obtained, the time evolution of the two-step pulse sequence is given in the form of $\Psi(\tau_{\rm total})=H_F(\tau_2')H_B(\tau_2)H_F(\tau_1')H_B(\tau_1)\Psi(0)$, where the Hamiltonian for free propagation is $H_F=-\frac{d^2}{dx^2}$. In order to optimize the pulse sequence, we assume that the initial condition is the zero-momentum state, although the initial wave packet contains nonzero momentum states. This approximation works well if the harmonic potential ν is loose and the interaction strength g is high. Since there is no accelerating force during the pulse sequence, we only consider the dynamics at $q=0$. This assumption allows us to use a fidelity $F=|\langle\phi_B(m,q=0)|\Psi(\tau_{\rm total})\rangle|^2$ as an informative index where m is a target band index. In this paper, our target states are the eigenstates of the Bloch Hamiltonian H_B with the phases $\phi_1=\phi_2=0$. During the on-duty cycle, we use the same lattice height s_1, s_2 for the target state; however, we vary ϕ_1, ϕ_2 for optimization.

TABLE V. Optimized loading protocols to the first and the second excited bands with two-step on-off procedure by using a brute force method with a period of 0.1 μs grid [24]. The lattice height s_1 is fixed to 10. In this paper, we chose a relative phase equal to $\pi/4$ for loading atoms to the antisymmetric solution.

ϕ_{11}	ϕ_{21}	ϕ_{12}	ϕ_{22}	τ_1	τ_1'	τ_2	τ_2'	F
$\pi/4$	$\pi/4$	$\pi/4$	$\pi/4$	33.8	34.7	14.8	4.5	0.939
0	0	$\pi/4$	$\pi/4$	12.7	34.6	1.5	16.9	0.966
$\pi/4$	$\pi/8$	$\pi/4$	$\pi/8$	32.8	39.9	39.9	6.5	0.967
0	0	$\pi/4$	$\pi/8$	29.0	18.2	0.1	4.9	0.957

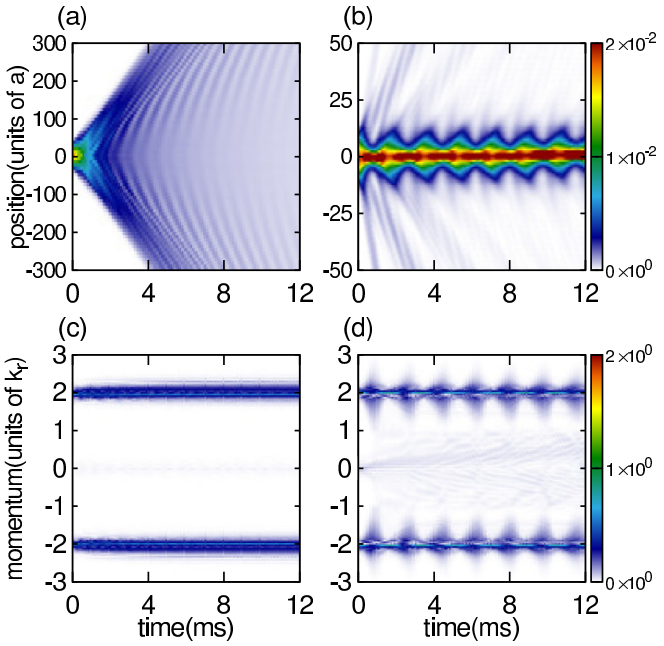

FIG. 13. Time propagation of the wave packet as a function of holding time with the normal band $s_1=10$, $s_2=5$ for $g=8$. The optimized loading protocol is shown in Table VI. (a) and (b) correspond to the density distributions in position space with symmetric (even-to-even) and antisymmetric (even-to-odd) loading process, respectively. (c) and (d) correspond to the momentum distributions after the band mapping for (a) and (b).

As seen in Fig. 1, the coefficients of the antisymmetric solutions in K space must have different signs for positive and negative indices K. And the off-duty cycle with the free Hamiltonian H_F gives a time-dependent phase change corresponding to the square of the momentum $e^{-4K^2\tau'}$ for each K momentum state. Therefore, to achieve loading atoms onto antisymmetric states, the on-duty cycle with H_B needs to choose appropriate phases ϕ_1, ϕ_2. For example, if we choose $\phi_1=\pi/4$ and $\phi_2=\pi/8$, the recurrent formula becomes

$$\begin{aligned}&(q+2K)^2C_B(n,q,K)+is_2C_B(n,q,K-2)/4\\&\quad+is_1C_B(n,q,K-1)/4-is_1C_B(n,q,K+1)/4\\&\quad-is_2C_B(n,q,K+2)/4\\&=\big(E_q^n-s_1/2-s_2/2\big)C_B(n,q,K).\end{aligned}\tag{A2}$$

In this case, the on-duty cycle gives phases for momentum states with negative K, which is opposite to the phases for positive K states. Besides, we need to vanish the $K=0$ components using an interference effect since the $K=0$ components of the antisymmetric state should be zero. Thus, the effect of the OL phases on the optimization is nontrivial. We numerically searched optimized time intervals by using a brute force method with a 0.1 μs step size in each of the time durations $0\leqslant\tau_1,\tau_1',\tau_2,\tau_2'\leqslant 40$ μs. We limit $\tau_{\rm total}\leqslant 100$ μs by following the previous studies [19–21,24,27]. To check the

TABLE VI. Optimized loading protocols with two-step on-off procedure for $s_1 = 10$, $s_2 = 5$. As in Table I, we chose relative phase equal to $\phi_{11} = \phi_{21} = \phi_{12} = \phi_{22} = \pi/4$ for antisymmetric loading for on-duty cycles.

Target	τ_1	τ_1'	τ_2	τ_2'	F
Second, even	3.8	4.9	23.1	28.9	0.999
First, odd	35.6	29.4	17.3	4.5	0.940

effect of the OL phases for loading atoms to the second excited band (antisymmetric solution), we chose 0, $\pi/4$, and $\pi/8$. See Table V for the results.

The result shows that $\phi_{11} = \phi_{21} = \pi/4$ and $\phi_{12} = \phi_{22} = \pi/8$ are the best choices for loading atoms to the second excited and the fidelity was found to be above 90% for all combinations. As for the experiments, it is better to choose the same phases $\phi_{11} = \phi_{12} = \phi_{21} = \phi_{22}$ to increase reproducibility, so, for simplicity, in this paper, we used $\phi_{11} = \phi_{12} = \phi_{21} = \phi_{22} = \pi/4$. We note that we used the zero phase for loading atoms to the first excited band (symmetric solution) since the $\phi_{11} = \phi_{12} = \phi_{21} = \phi_{22} \neq 0$ lowers the fidelity for loading. For detailed discussions on the effects of the parabolic trap, see our previous paper [24].

APPENDIX B: LOADING PROCESS WITH THE NORMAL BAND

In this section, we briefly discuss a selection rule of the loading process with the normal band ($s_1 = 10$, $s_2 = 5$). Here, we numerically examine the loading process to the first excited (even to odd) and second excited (even to even) band with $g = 8$.

In the case of normal dispersion, at $q = 0$, the first excited band solution is antisymmetric, and the second excited band is symmetric. Therefore, in the linear limit, the loading process with the relative phases $\phi_{11} = \phi_{21} = \phi_{12} = \phi_{22} = 0$ can load atoms to the second excited band. Figure 13 shows the time evolution immediately after the loading process. Both of the processes load atoms to around $|p| = 2$ in momentum space [Figs. 13(c) and 13(d)]. In position space, contrary to the case of the inverted band, the loading to the antisymmetric solutions produces the solitonic state. We also numerically confirmed that the trend is unchanged in the monochromatic lattice limit ($s_2 = 0$, normal band). The results for $s_1 = 10$, $s_2 = 0$ are not shown since it is similar to the case of $s_1 = 10$, $s_2 = 5$. In this Appendix, we just checked the validity of the pulse-sequence procedure. Therefore, further research is needed on the properties of solitons in the normal band, such as dynamical instabilities.

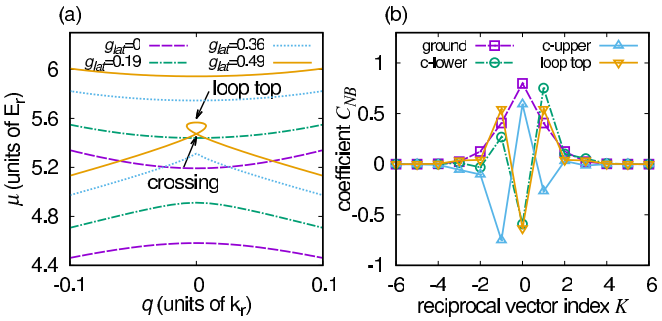

FIG. 14. (a) Band structure around first and second excited bands. Purple dashed, green dash-dotted, light blue short dashed, and orange solid lines correspond to $g_{\rm lat} = 0$, 0.19, 0.36, and 0.49. The interaction term gradually modifies the band structure, and the loop appears at a point a little short of $g_{\rm lat} = 0.4$. (b) The first four Bloch coefficients for $g_{\rm lat} = 0.49$. The coefficients at the crossing point (referred to as "c-lower" and "c-upper") are a superposition of an even and odd symmetry solution. The solution at the top of the loop has even symmetry.

APPENDIX C: LOOP STRUCTURE IN BICHROMATIC OL

This Appendix considers the loop formation in the band structure with the nonlinear bichromatic OL. Here we use the lattice height $s_1 = 10$, $s_2 = 8$, the same as in the main discussion.

Figure 14(a) shows the band structure around the first and second excited bands with $s_1 = 10$, $s_2 = 8$ for four values of $g_{\rm lat}$. As a precursor to the emergence of the loop, the derivative of the band dispersion $\frac{d\mu(q)}{dq}$ becomes discontinuous at $q = 0$, if $g_{\rm lat} = 0.36$. When $g_{\rm lat}$ is greater than 0.4, the solution of the first excitation band at $q = 0$ is split into three parts: two degenerate solutions and a loop top solution. Then the loop appears at $q = 0$ as seen in Fig. 1(b).

Figure 14(b) shows the first four NBW coefficients $C_{NB}(n, q, K)$ with $g_{\rm lat} = 0.49$. The solution at the ground band has the same symmetry as in the linear case [see Fig. 1(d)]. Two additional solutions at the crossing point consist of a superposition of odd and even symmetric solutions. At the loop, the solution reflects the symmetry of the linear solution, which has a large overlap with the linear one. We numerically checked that this trend remains unchanged up to $g_{\rm lat} = 1$ [see Fig. 1(a)]. This result suggests that it is possible to load atoms onto the loop top by the pulse-sequence method; however, it is necessary to discuss how the degenerate solutions affect the loading process.

[1] O. Morsch and M. Oberthaler, Rev. Mod. Phys. **78**, 179 (2006), and references therein.
[2] F. Lederer, G. I. Stegeman, D. N. Christodoulides, G. Assanto, M. Segev, and Y. Silberberg, Phys. Rep. **463**, 1 (2008), and references therein.
[3] H. Deng, H. Haug, and Y. Yamamoto, Rev. Mod. Phys. **82**, 1489 (2010), and references therein.
[4] M. Machholm, C. J. Pethick, and H. Smith, Phys. Rev. A **67**, 053613 (2003).
[5] Biao Wu and Qian Niu, New J. Phys. **5**, 104 (2003)
[6] C. Chin, R. Grimm, P. Julienne, and E. Tiesinga, Rev. Mod. Phys. **82**, 1225 (2010).
[7] A. L. Marchant, T. P. Billam, T. P. Wiles, M. M. H. Yu, S. A. Gardiner, and S. L. Cornish, Nat. Commun. **4**, 1865 (2013).

[8] J. H. V. Nguyen, P. Dyke, De Luo, B. A. Malomed, and R. G. Hulet, Nat. Phys. **10**, 918 (2014).

[9] T. Mežnaršič, T. Arh, J. Brence, J. Pišljar, K. Gosar, Žiga Gosar, Rok Žitko, E. Zupanič, and P. Jeglič, Phys. Rev. A **99**, 033625 (2019).

[10] J. Polo and V. Ahufinger, Phys. Rev. A **88**, 053628 (2013); J. L. Helm, S. L. Cornish, and S. A. Gardiner, Phys. Rev. Lett. **114**, 134101 (2015); H. Sakaguchi and B. A. Malomed, New J. Phys. **18**, 025020 (2016).

[11] H. Sakaguchi and B. A. Malomed, J. Phys. B: At. Mol. Opt. Phys. **37**, 1443 (2004).

[12] D. E. Pelinovsky, A. A. Sukhorukov, and Y. S. Kivshar, Phys. Rev. E **70**, 036618 (2004).

[13] Y. Zhang and B. Wu, Phys. Rev. Lett. **102**, 093905 (2009); Y. Zhang, Z. Liang, and B. Wu, Phys. Rev. A **80**, 063815 (2009).

[14] K. Winkler, O. A. Egorov, I. G. Savenko, X. Ma, E. Estrecho, T. Gao, S. Müller, M. Kamp, T. C. H. Liew, E. A. Ostrovskaya, S. Höfling, and C. Schneider, Phys. Rev. B **93**, 121303(R) (2016).

[15] C. Bersch, G. Onishchukov, and U. Peschel, Phys. Rev. Lett. **109**, 093903 (2012).

[16] S. B. Koller, E. A. Goldschmidt, R. C. Brown, R. Wyllie, R. M. Wilson, and J. V. Porto, Phys. Rev. A **94**, 063634 (2016)

[17] S. Masuda, K. Nakamura, and M. Nakahara, New J. Phys. **20**, 025008 (2018).

[18] E. J. Halperin, M. W. C. Sze, J. P. Corson, and J. L. Bohn, Phys. Rev. A **100**, 013608 (2019).

[19] Y. Zhai, X. Yue, Y. Wu, X. Chen, P. Zhang, and X. Zhou, Phys. Rev. A **87**, 063638 (2013).

[20] Z. Wang, B. Yang, D. Hu, X. Chen, H. Xiong, B. Wu, and X. Zhou, Phys. Rev. A **94**, 033624 (2016).

[21] X. Zhou, S. Jin, and J. Schmiedmayer, New J. Phys. **20**, 055005 (2018).

[22] J. Hecker Denschlag, J. E. Simsarian, H. Häffner, C. McKenzie, A. Browaeys, D. Cho, K. Helmerson, S. L. Rolston, and W. D. Phillips, J. Phys. B: At. Mol. Opt. Phys. **35**, 3095 (2002).

[23] D. Hu, L. X. Niu, S. J. Jin, X. Z. Chen, G. J. Dong, J. Schmiedmayer, and X. J. Zhou, Commun. Phys. **1**, 29 (2018).

[24] T. Yamakoshi and S. Watanabe, Phys. Rev. A **99**, 013621 (2019).

[25] A. Görlitz, T. Kinoshita, T. W. Hänsch, and A. Hemmerich, Phys. Rev. A **64**, 011401(R) (2001); M. Weitz, G. Cennini, G. Ritt, and C. Geckeler, *ibid.* **70**, 043414 (2004); G. Ritt, C. Geckeler, T. Salger, G. Cennini, and M. Weitz, *ibid.* **74**, 063622 (2006).

[26] B. Yang, S. Jin, X. Dong, Z. Liu, L. Yin, and X. Zhou, Phys. Rev. A **94**, 043607 (2016).

[27] D. Hu, L. Niu, B. Yang, X. Chen, B. Wu, H. Xiong, and X. Zhou, Phys. Rev. A **92**, 043614 (2015).

[28] T. Yamakoshi and S. Watanabe, Phys. Rev. A **91**, 063614 (2015).

[29] T. Yamakoshi, F. Saif, and S. Watanabe, Phys. Rev. A **97**, 023620 (2018).

[30] M. Olshanii, Phys. Rev. Lett. **81**, 938 (1998).

[31] C. Kittel, *Introduction to Solid State Physics 8th Edition* (Wiley, New York, 2004).

[32] Y. Chen, L.-B. Fu, and Y. Chen, Physica A **390**, 1033 (2011); Y. Kominis and K. Hizanidis, Opt. Express **16**, 12124 (2008).

[33] D. J. Tannor, *Introduction to Quantum Mechanics* (University Science Book, Herndon, VA, 2007).

[34] M. A. Kristensen, M. Gajdacz, P. L. Pedersen, C. Klempt, J. F. Sherson, J. J. Arlt, and A. J. Hilliard, J. Phys. B: At. Mol. Opt. Phys. **50**, 034004 (2017).

[35] H. Ott, Rep. Prog. Phys. **79**, 054401 (2016).

[36] R. Yamamoto, J. Kobayashi, K. Kato, T. Kuno, Y. Sakura, and Y. Takahashi, Phys. Rev. A **96**, 033610 (2017).

[37] M. Greiner, I. Bloch, O. Mandel, T. W. Hänsch, and T. Esslinger, Phys. Rev. Lett **87**, 160405 (2001); M. Köhl, H. Moritz, T. Stöferle, K. Günter, and T. Esslinger, *ibid.* **94**, 080403 (2005)

[38] J. Heinze, J. S. Krauser, N. Fläschner, B. Hundt, S. Götze, A. P. Itin, L. Mathey, K. Sengstock, and C. Becker, Phys. Rev. Lett. **110**, 085302 (2013).

[39] J. F. Sherson, S. J. Park, P. L. Pedersen, N. Winter, M. Gajdacz, S. Mai, and J. Arlt, New J. Phys. **14**, 083013 (2012); P. L. Pedersen, M. Gajdacz, N. Winter, A. J. Hilliard, J. F. Sherson, and J. Arlt, Phys. Rev. A **88**, 023620 (2013).

[40] D. Witthaut, T. Salger, S. Kling, C. Grossert, and M. Weitz, Phys. Rev. A **84**, 033601 (2011).

[41] T. Salger, C. Grossert, S. Kling, and M. Weitz, Phys. Rev. Lett. **107**, 240401 (2011).

[42] M. Matuszewski, W. Królikowski, M. Trippenbach, and Y. S. Kivshar, Phys. Rev. A **73**, 063621 (2006).

[43] A. Eckardt, Rev. Mod. Phys. **89**, 011004 (2017), and references therein.

[44] S. Kling, T. Salger, C. Grossert, and M. Weitz, Phys. Rev. Lett. **105**, 215301 (2010).

[45] N. Fläschner, M. Tarnowski, B. S. Rem, D. Vogel, K. Sengstock, and C. Weitenberg, Phys. Rev. A **97**, 051601(R) (2018).

[46] S. J. Park, H. K. Andersen, S. Mai, J. Arlt, and J. F. Sherson, Phys. Rev. A **85**, 033626 (2012).

[47] T. Yamakoshi, S. Watanabe, S. Ohgoda, and A. P. Itin, Phys. Rev. A **93**, 063637 (2016).

[48] J. T. Cole and Z. H. Musslimani, Phys. Rev. A **90**, 013815 (2014).

[49] S. Masuda, K. Nakamura, and A. D. Campo, Phys. Rev. Lett. **113**, 063003 (2014); S. Martínez-Garaot, M. Palmero, J. G. Muga, and D. Guéry-Odelin, Phys. Rev. A **94**, 063418 (2016).

[50] T. F. Xu, X. M. Guo, X. L. Jing, W. C. Wu, and C. S. Liu, Phys. Rev. A **83**, 043610 (2011).

[51] M. Holthaus, J. Phys. B: At. Mol. Opt. Phys. **49**, 013001 (2016).

[52] C. J. Fujiwara, K. Singh, Z. A. Geiger, R. Senaratne, S. V. Rajagopal, M. Lipatov, and D. M. Weld, Phys. Rev. Lett. **122**, 010402 (2019).

[53] L. Wang, M. Troyer, and X. Dai, Phys. Rev. Lett. **111**, 026802 (2013); S. Nakajima, T. Tomita, S. Taie, T. Ichinose, H. Ozawa, L. Wang, M. Troyer, and Y. Takahashi, Nat. Phys. **12**, 296 (2016); M. Lohse, C. Schweizer, O. Zilberberg, M. Aidelsburger, and I. Bloch, *ibid.* **12**, 350 (2016).

[54] Y. Zhang, Y. Xu, and T. Busch, Phys. Rev. A **91**, 043629 (2015).

[55] G. Watanabe and Y. Zhang, Phys. Rev. A **98**, 013625 (2018).